Journal of Materials Chemistry C

Multiconfigurational Dynamics Explain Photochemical Reactivity and Torquoselectivity Towards Fluorinated Polyacetylenes

Journal:	*Journal of Materials Chemistry C*
Manuscript ID	TC-ART-03-2020-001298.R1
Article Type:	Paper
Date Submitted by the Author:	21-May-2020
Complete List of Authors:	Cox, Jordan; Northeastern University College of Science, Chemistry & Chemical Biology Lopez, Steven; Northeastern University College of Science, Chemistry & Chemical Biology;

Multiconfigurational Dynamics Explain Photochemical Reactivity and Torquoselectivity Towards Fluorinated Polyacetylenes

Jordan M. Cox and Steven A. Lopez*

Department of Chemistry and Chemical Biology, Northeastern University, Boston, MA 02115

Abstract

The discovery of the conductivity of polyacetylene ignited the field of organic electronic materials. Functionalizing polyacetylenes with electron withdrawing groups (*e.g.*, fluorine), has theoretically been shown to increase the air-stability of PAs and open new avenues in organic electronics. Burns and coworkers recently reported a novel synthetic route to fluorinated polyacetylenes which utilizes as a key step the completely stereoselective photochemical electrocyclic ring-closing of hexafluorinated dienes. This photochemical torquoselective (*photo-torquoselective*) reaction is, to our knowledge, the first of its kind. While the torquoselectivity model (Houk and co-workers) describes the stereospecificity of thermal electrocyclic reactions, no such reactivity model exists for their photochemical counterpart. We have used multiconfigurational quantum chemical calculations and *ab initio* molecular dynamics simulations to describe this reaction and to determine the origin of its stereoselectivity. We show that the reaction proceeds through the S_1 excited state with a half-life of 445 fs. This reaction lies along an energetically unfavorable pathway which results in a reaction quantum yield of approximately 14%. We predict that the reaction pathway to the unobserved product lies as much as 0.3 eV (6.9 kcal mol^{-1}) higher in energy than the pathway to the observed isomer. The reaction pathway to the observed product benefits from stabilizing $F^{\delta-}\ldots H^{\delta+}$ interactions while the pathway to the unobserved product suffers from destabilizing F−F closed-shell repulsion. The combination of these two stereoelectronic effects is responsible for the difference in energy between the two pathways which directs the reaction exclusively to the observed product.

Introduction

π-Conjugated organic molecules and polymers are components of organic semiconductors (OSCs) that have become increasingly important for organic electronics. Organic electronic materials function in large part due to the excellent charge transport properties of planar π-conjugated materials. These materials are of interest for organic electronic devices, such as organic light-emitting diodes (OLEDs) and organic field-effect transistors (OFETs),[1] and organic photovoltaics (OPVs).[2, 3] Organic materials are particularly attractive because their structures, photophysical properties, and bulk properties can be rationally tuned with substituent effects and π-conjugation. The mobilities of OFETs are now competitive with amorphous silicon[4] with field effect mobilities of 0.1−1 $cm^2\ V^{-1}\ s^{-1}$, which has made the advent of curved displays[5-8] and sensors[9-11] possible.

Many of the highest performing OFETs are comprised of molecular single crystals. Single-crystals of pentacene and rubrene, for example, have been shown to have hole mobilities of 1.4 and 10.7 $cm^2\ V^{-1}\ s^{-1}$ [12]; electron mobility in amorphous silicon is approximately 3 $cm^2\ V^{-1}\ s^{-1}$.[13] While charge mobilities and conductivity in these single-crystalline materials may be high, they pose challenges to both manufacturing and flexible device applications[14], as single-crystals are rigid and brittle compared to polymer and plastic materials. This has sparked significant interest in the development of plastic organic electronics, which utilize semiconducting organic polymers.

Organic polymers continue to play a major role in the improvement of organic electronic materials, including solar cells,[15, 16] smart windows,[17, 18] and flexible electronic displays.[19, 20] The discovery of the high conductivity[21] of doped polyacetylene (PA) ignited the field of organic electronics, leading to the development and commercialization of numerous conductive polymers including polyaniline[22], poly(ethylenedioxythiophene) (PEDOT)[23], and polythiophene.[24] However, PA itself is difficult to process because it readily reacts with ambient oxygen and reduces the polymer's conductivity.[25] This instability has prevented commercial use of PA in organic electronics. Early reports[26-28] suggest that functionalizing PA with electron-withdrawing substituents (*e.g.* fluorine) will lower the energy of the highest occupied bands (Fermi level), thus slowing the reaction with O_2. While a perfluorinated PA has not yet been reported, Burns and coworkers recently published the first synthesis of a partially fluorinated PA. Scheme 1 shows the photochemical cascade reaction used to synthesize fluorinated ladderenes, which are efficiently polymerized with a ring-opening metathesis polymerization (ROMP). A subsequent mechanochemical *unzipping* of the polyladderenes affords fluorinated PA.[29, 30]

Scheme 1. Synthesis of all-anti hexafluoro-[5]-ladderene **3** via photochemical cascade reaction. Reaction proceeds through isolable intermediate **2** to yield **3** in 57% yield, while the *syn* isomer is unobserved.

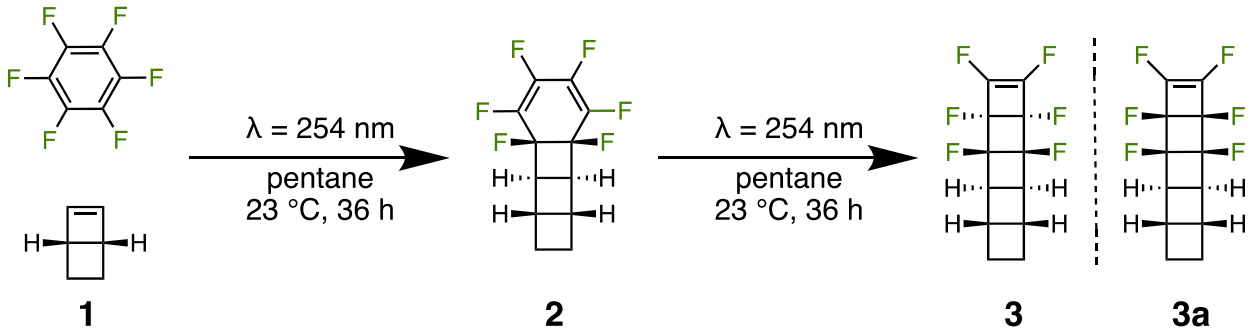

The photochemical 4π electrocylic ring closing in this photochemical cascade is disrotatory as dictated by the Woodward-Hoffman rules.[31] The reaction is completely stereoselective and affords a single diastereomer, **3**. To the best of our knowledge, this reaction shown in Scheme 1 is the first example of a photochemical torquoselective (*photo-torquoselective*) reaction reported in the literature. Thermal 4π conrotatory electrocyclic ring closing reactions have been extensively reported in the literature and have been leveraged as the key transformation in the syntheses of the following natural products: (±)-tetrapetalone A-Me aglycon,[32] taiwaniaquinone H,[33] (±)-methyl rocaglate,[34] (±)-rocaglamide,[35] cribrostatin 6,[36] (±)-cephalotaxine,[37] (±)-roseophilin,[38] nakiterpiosin,[39] (±)-merrilactone A,[40] (−)-scabronine G[41]. These reactions feature substituents that appear to rotate "outward" or "inward" during the electrocyclic reaction. The preference for the substituent(s) to rotate "inward" or "outward" is known as torquoselectivity, a concept first described by Houk and co-workers in the 1980s.[42-47] This work describes the nature of the photoexcitation and subsequent stereoselective photochemistry of **2**. To this end, we have used multiconfigurational quantum chemical calculations and 1 picosecond *ab initio* molecular dynamics to understand the origin of the observed photo-torquoselectivity.

Results and Discussion

Photochemical reactions begin with the absorption of a photon, which promotes a vertical excitation of the reactant(s) into the Franck-Condon (FC) region[48] on a higher energy potential energy surface of the same multiplicity. Computational chemistry is an important tool that can be leveraged to describe the nature of the dominant transitions and their excitation energies. Many methods for computing these quantities generate electronic states as "excitations" from some ground-state reference electronic configuration. These methods are referred to as single-reference or single-determinant methods; here we use time-dependent density functional theory (TD-DFT). TD-DFT is well suited to describing ground and excited states when those states are each well described by a single electronic configuration, but does not account for doubly-excited configurations and cannot correctly describe the potential energy surface (PES) topology near surface crossings.[49] Multiconfigurational methods then are vital to the correct description of the electronic structure. One example is complete active space self-consistent field (CASSCF). CASSCF accounts for contributions from multiple electronic configurations by allowing the average occupancy of a subset of the orbitals, called the active space, to vary from 0 to 2. CASSCF calculations require the selection of this active space; here we have selected the 4 electron, 4 orbitals active space shown by the boxed subset of orbitals in Figure 1.

These 4 orbitals describe the π-system of the diene, **2**, while the remaining 4 orbitals of the complete 8 electron, 8 orbital active space we have used previously,[30] comprise the σ-bonds formed during the initial [2+2] cycloaddition step. These additional orbitals do not contribute

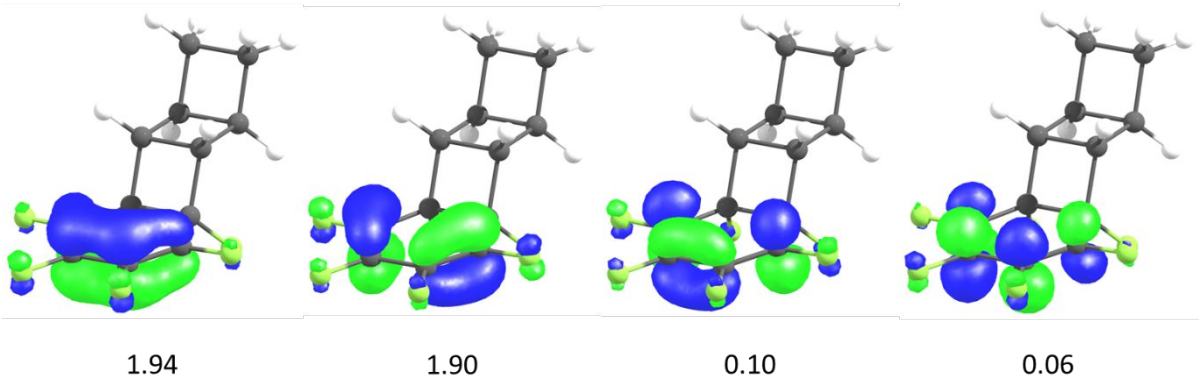

Figure 1. Active-space orbitals for **2** and their average occupancies in the ground-state wavefunction. Orbitals were computed at the CASSCF(4,4)/ANO-S-VDZP level. Isovalue = 0.075.

significantly to the multiconfigurational character of the wavefunction during the ring-closing step, and have therefore been omitted from our active space here.

We have optimized the ground state structure of **2** with CASSCF(4,4) and an ANO-S-VDZP basis set[50], and state-averaging over the lowest three states (SA-3-CASSCF(4,4)/ANO-S-VDZP). We then computed the vertical excitation energy of **2** with several single- and multiconfigurational quantum mechanical single point energy calculations. Figure 2 shows a summary of the computed vertical excitation energies using TD-CAM-B3LYP[51] and complete active space self-consistent field (CASSCF)[52] with and without a second-order perturbative energy correction using the

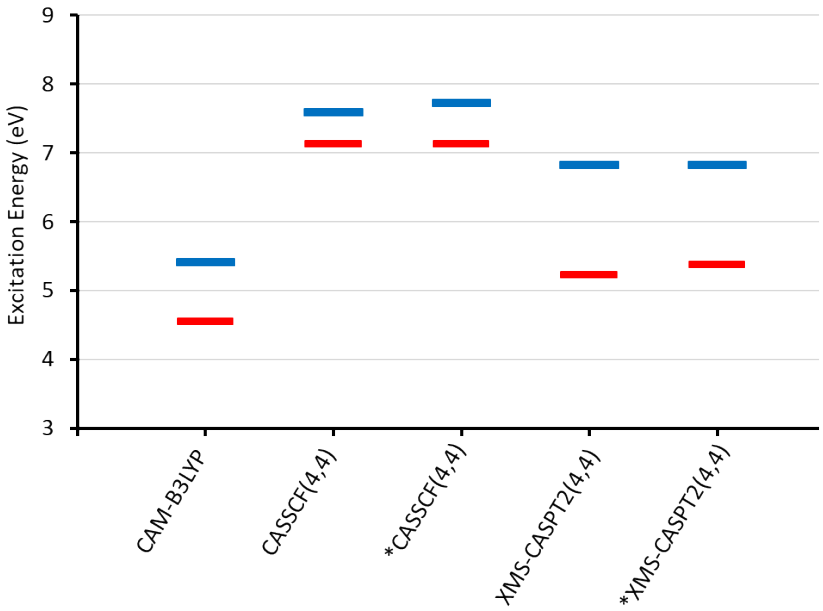

Figure 2. S_1 (red) and S_2 (blue) vertical excitation energies of **2** as computed by various methods. Methods marked with * were computed with the ANO-S-VDZP basis set, all other energies were computed with the aug-cc-PVDZ basis set. All calculations were performed using the geometry of **2** optimized at the CASSCF(4,4)/ANO-S-VDZP level.

extended multistate formalism (XMS-CASPT2).[53, 54] The contributions of various electronic configurations and computed oscillator strengths are shown in the Supporting Information (Table S1). A discussion of the various methods is provided in the Computational Methods section. TD-CAM-B3LYP predicts that the S_1 excited state is dominated by a singly-excited highest occupied molecular orbital to lowest unoccupied molecular orbital (HOMO→LUMO) ππ* configuration (Table S1). In the case of excited states which are well described by a single electronic configuration, single-configurational methods like TD-CAM-B3LYP can predict excitation energies to within 0.4 eV with a large (triple- or quadruple-zeta) basis set.[55, 56] Figure 2 shows that CAM-B3LYP predicts an excitation energy to S_1 of 4.55 eV. CAM-B3LYP has been shown to often underestimate vertical excitation energies in organic molecules[56], and it is known that the errors in CAM-B3LYP excitation energies are not systematic with respect to basis set size.[57] It is no surprise then that the CAM-B3LYP excitation energy is 0.67 eV lower than XMS-CASPT2.

To confirm that our selected active space is appropriate, we must first ensure that it can correctly describe the electronic states involved in the reaction. With our selected (4,4) active space, CASSCF predicts that the S_1 state has ππ* character as predicted by TD-CAM-B3LYP, but it also contains significant contributions from several other singly- and doubly-excited configurations. It also predicts an excitation energy of 7.13 eV, an overestimation of 1.91 eV compared to XMS-CASPT2 which predicts the excitation energy to be 5.22 eV. The discrepancies between CASSCF and the TD-CAM-B3LYP and XMS-CASPT2 results are due in large part to the absence of dynamic electron correlation in CASSCF, an effect which is well established in the literature[58-63] and which is recovered by the perturbation correction in XMS-CASPT2.

XMS-CASPT2 predicts the S_1 state should have the same ππ* nature as predicted by TD-CAM-B3LYP, and eliminated the contributions from other configurations. To within the relative errors

of the methods, the XMS-CASPT2 results agree well that of TD-CAM-B3LYP, which indicates that our active space is sufficient to describe the electronic structure of 2. However, because CASSCF introduces some error due to the inclusion of additional electronic configurations, we must verify that CASSCF qualitatively reproduces the XMS-CASPT2 potential energy surface (PES).

Reaction Coordinate Diagram

To describe the PES topology throughout the course of the photochemical reaction **2**, we optimized a minimum-energy crossing point (MECP) between the S_1 and S_0 PESs at the CAS(4,4)/ANO-S-VDZP level. We then computed reaction coordinate energy diagrams from a linear interpolation of geometries from **2** to the relevant MECP geometry and from the MECP to the products, as inspired by a report by Martínez and co-workers.[64] Figure 3 shows the reaction coordinate diagram computed at the SA-3-CASSCF(4,4)/ANO-L-VTZP and XMS-CASPT2(4,4)/ANO-L-VTZP levels of theory for the formation of **3** (black and red) and **3a** (gray and pink).

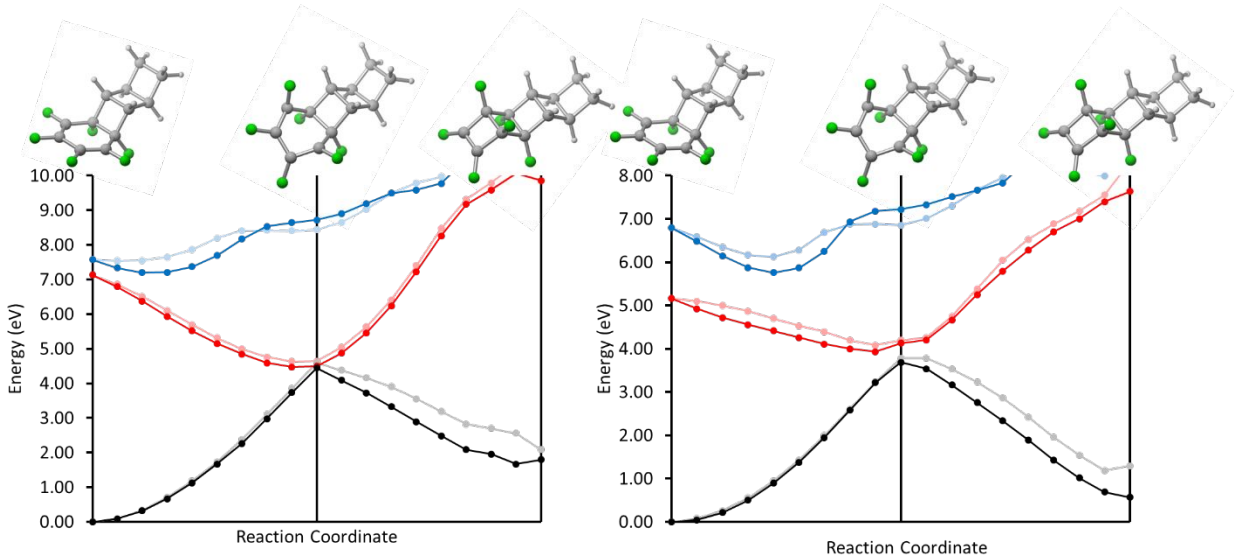

Figure 3. Reaction coordinate diagram for the electrocyclic ring closing of **2** generated by interpolation of the redundant internal coordinates*, computed at the SA-3-CASSCF(4,4)/ANO-L-VTZP (left) and XMS-CASPT2(4,4)/ANO-L-VTZP (right) level. Black and red traces show the S_0 and S_1 energies, respectively, along the reaction coordinate towards **3**. Gray and pink traces show the S_0 and S_1 energies, respectively, along the reaction coordinate towards the unobserved **3a**.

The CASSCF diagram (left of Figure 3) qualitatively matches the XMS-CASPT2 results (right of Figure 3). The higher accuracy of the XMS-CASPT2 energies suggests that, despite the errors introduced by CASSCF, the conclusions we can draw from the CASSCF calculations and dynamics simulations are reliable. Both methods show an energetically downhill relaxation pathway from the Franck-Condon point to a shallow excited-state low-energy region towards both **3** and **3a**. **3a** corresponds to a reaction pathway [1]that is between 0.2 and 0.3 eV (5−7 kcal mol^{-1})

*Note: Interpolated geometries in these diagrams are not optimized. Any energetic barrier that appears in these diagrams should be interpreted as an upper bound to the true energy barrier value, if such a barrier exists at all.

higher in energy than the pathway leading to **3**. There are some key differences between these surfaces, however, which are important to note as well. The CASSCF surface shows a much steeper slope of the S_1 surface between the reactant and the MECP, compared to XMS-CASPT2, due to the overestimation of the vertical excitation energy. Also, CASSCF underestimates the energy difference between the *anti* and *syn* pathways in this same PES region. Therefore, in subsequent dynamics simulations using CASSCF, we expect that this method may underestimate the selectivity of the reaction compared to experiment.

The CASSCF diagram suggests that there may be a shallow energetic minimum before the MECP in both the *syn* and *anti* pathways. We have optimized these minima at the SA-3-CASSCF(4,4)/ANO-S-VDZP level, and they lie less than 0.08 eV below the MECP energy, an easily traversable barrier. The energy difference between the two possible reaction pathways suggests that photoexcited molecules of **2** will tend to initially relax towards **3**, though the reaction path towards **3a** may still be accessible.

Ab initio molecular dynamics simulations

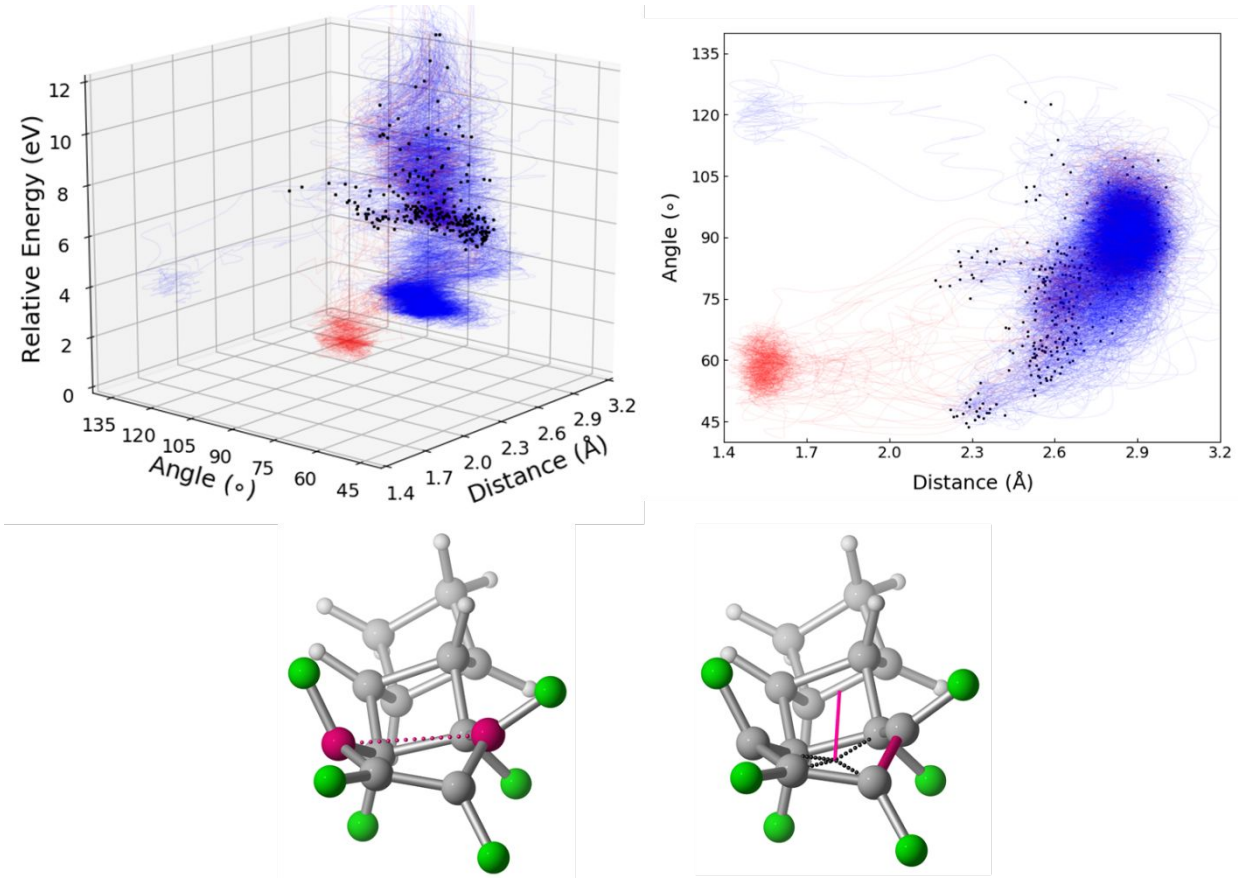

Figure 4. Perspective view (top-left) and top view (top-right) of the plot of the time evolution of 256 FSSH trajectories initialized in the S_1 state. **MECP-*anti*** (bottom) with geometric parameters highlighted. Reactive C–C distance (bottom-left) and out-of-plane angle (bottom-right). Initial conditions were generated from a Wigner distribution of the ground state minimum. Trajectories were propagated for 1 ps at 300 K with a 1.0 fs time step. Black circles show S_1/S_0 hopping points of each trajectory. Red traces are trajectories which formed the experimentally observed product, **3**.

Towards our goal of understanding the origin of the photochemical stereoselectivity of the 4π electrocyclic ring closing of **2**, we simulated the reaction by performing 256 *ab initio* [CASSCF(4,4)/ANO-S-VDZP] molecular dynamics simulations for 1 picosecond. We used Tully's fewest-switches surface-hopping (FSSH) algorithm[65] at 300 K with a 1.0 fs timestep, after performing a Wigner sampling of the reactant, **2**. At the end of the dynamics simulations, we examined the nature of the active space orbitals by visual inspection of the final orbitals and an in-house analysis script that examines the entire trajectory to ensure the integrity of the active space throughout the simulations. We found that the active space orbitals for product-yielding trajectories smoothly transition to the expected π/π* and σ/σ* orbitals of the products.

Of the 256 1 ps trajectories, 97.7% (250) of these surface-hopping trajectories reached the ground state within the simulation time. Figure 4 shows the time evolution of these trajectories from their initial geometries in the Franck-Condon region of the S_1 surface to their final ground-state geometries. The progress of these trajectories is plotted as a function of two key geometric parameters, the reactive C−C distance (1,4 carbons of the diene) and the out-of-plane angle, defined as the angle between the cyclohexadiene plane normal and the bond between one reactive carbon atom and the adjacent sp^2 carbon, shown in the bottom of Figure 4.

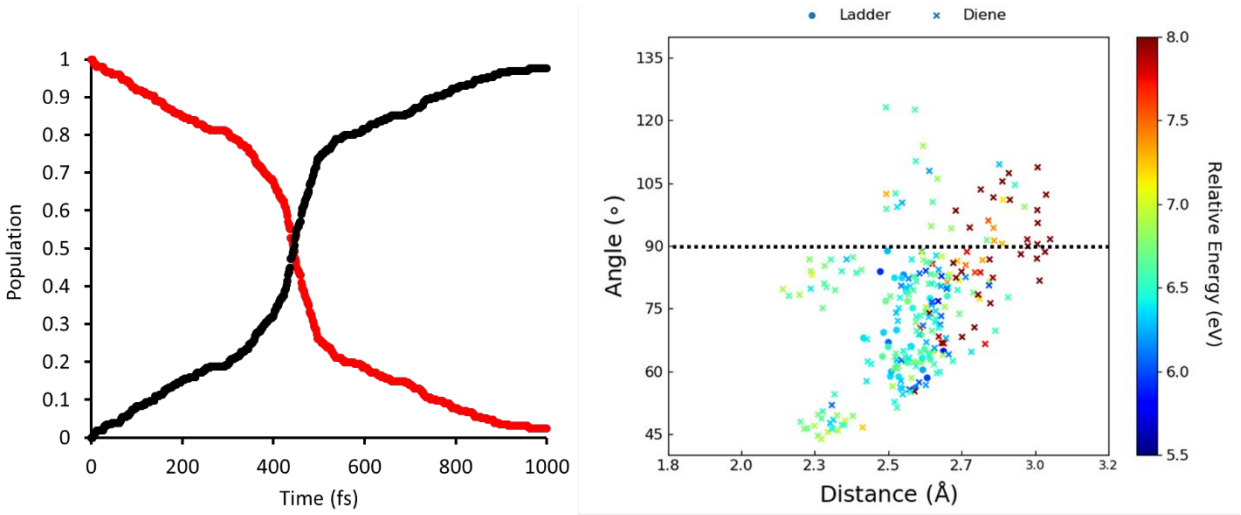

Figure 5. (Left) Time evolution of the average population of S1 (red) and S0 (black) for 256 FSSH trajectories. (Right) Plot of S_1/S_0 hopping points for 250 FSSH trajectories. Hopping points for trajectories that led to the formation of **3** are represented by circles, all other trajectories are shown as 'X's.

Upon photoexcitation, the trajectories initially relax from the Franck-Condon region, dispersing across the excited-state PES, before converging back onto a lower-energy region of the excited-state surface, shown by the upper dark-blue region with energies near 5 eV in Figure 4. The large concentration of S_1/S_0 hopping points in this region, shown by the black circles in Figure 4, shows that the majority of trajectories relax into this excited-state region before hopping to the ground state. During the 1 ps simulation time 250 (97.7%) of the trajectories crossed to the ground state, and 37 (14.5%) went on to form the ladderene photoproduct. Interestingly, three of these ladderenes were the experimentally unobserved **3a**. The left half of Figure 5 shows the time evolution of the relative populations of the S_0 and S_1 states. The population decay from the S_1 state shows a sigmoidal shape and a half-life of 445 fs.

We then analyzed what is known as the hopping point of each trajectory, the point along each trajectory when the molecule hops from the S_1 state to the S_0. The right side of Figure 5 shows a plot of the time evolution of the S_1 and S_0 population and the 250 trajectory hopping points. The hopping point plot shows that the majority of trajectories (85%) hop to the ground state with an out-of-plane angle ≤ 90°, which corresponds to a geometry that resembles **MECP-*anti*** and the observed product **3**. This suggests that as the trajectories evolve on the excited state surface, they are more often in a geometry pre-distorted towards the favored (all-*anti*) product. As the energy of the hopping points decreases there is an increasing preference for *anti*-pre-distorted geometries

The 34 trajectories that led to **3** are represented by circles; they hop to the ground state near **MECP-*anti***. However, unlike the other hopping points in this same region of the PES, they are the only three trajectories with hopping point energies which are significantly higher than the MECP, lying at 0.61, 0.77, and 1.16 eV above the MECP energy. This suggests that product formation requires crossing to the ground state at some high energy portion of the S_1/S_0 crossing seam, away from the MECP.

MECP Branching Planes

Our computed reaction coordinate diagrams show that the relaxation pathway from both **MECP-*syn*** and **MECP-*anti*** to the corresponding product should be facile and downhill. This contradicts our dynamics simulations that predict a reaction quantum yield of less than 15%. This suggests that the topography of the PES near the MECP is critical to determining the outcome of each trajectory. We have therefore computed the PES in the vicinity of the MECP branching plane (Figure 6a) for both **MECP-*syn*** and **MECP-*anti***. This plane is defined by two orthogonal vectors, the two unique normal mode vectors which lift the S_1/S_0 degeneracy, shown in the Supporting Information. Radial slices of these PESs are shown for clarity in Figure 6b. The differences in the PES topography are small but significant. **MECP-*syn*** is characterized as sloped single-path, according to the *P* and *B* conical intersection (CI) characterization parameters implemented in OpenMolcas.[66] In this case, all paths away from the CI point will curve towards a single direction. **MECP-*anti***, however, is characterized as sloped, bifurcating, meaning there are two unique paths of steepest descent away from the MECP.

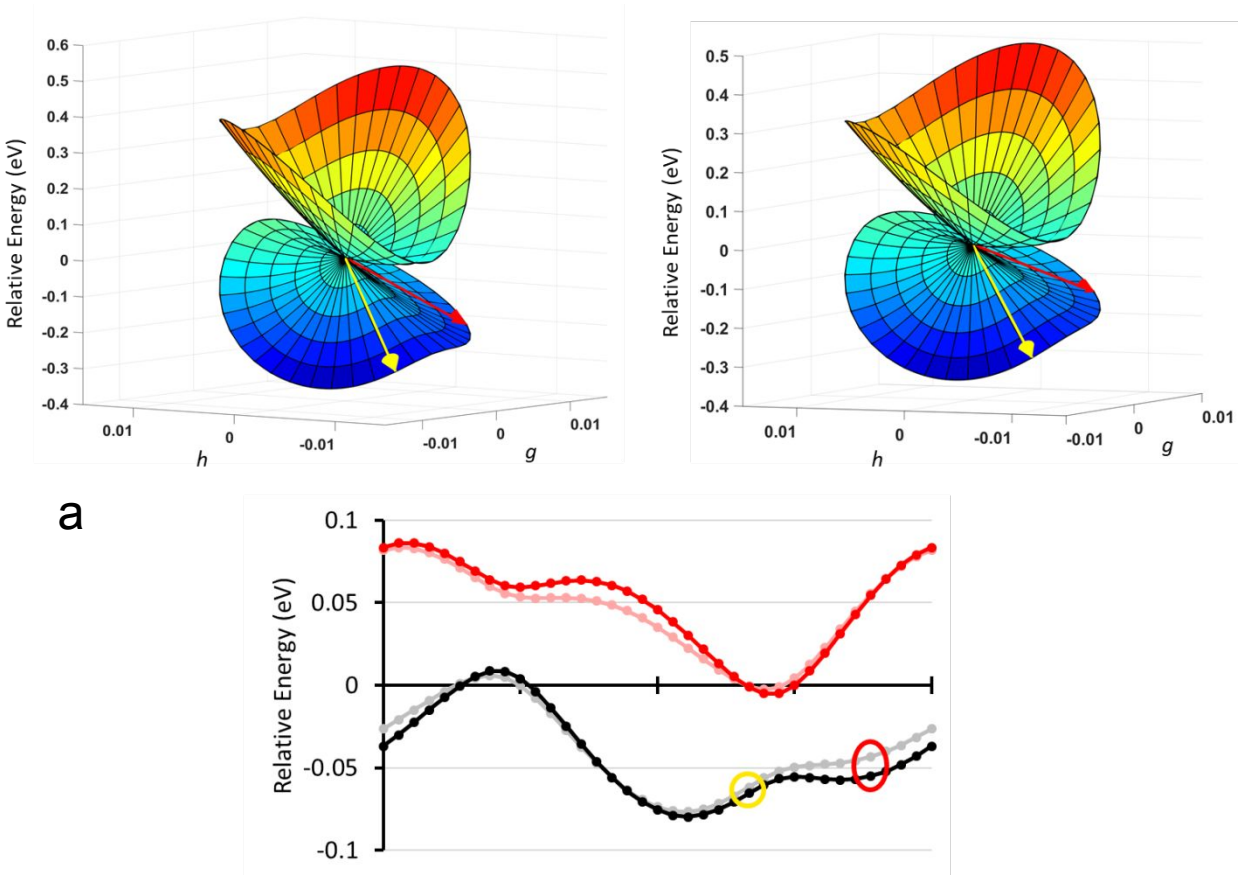

Figure 6. a) PES near **MECP-*anti*** (left) and **MECP-*syn*** (right). Yellow arrows indicate the reaction vector which leads towards the reactant diene **2**. Red arrows indicate the reaction vector that leads to the corresponding product, **3** (left) or **3a** (right). b) Radial slices of PESs in panel a. Yellow and red circles show the same reaction vectors as the arrows in panel a. Vectors *g* and *h* which define these branching spaces are shown in the Supporting Information. All energies are shown relative to the respective MECP energy.

The two vectors on each branching space plot in Figure 6a represent reaction vectors from the MECP towards the relevant product (**3** or **3a**) and reactant (**2**), in red and yellow respectively. Conceptually, they are directions in the branching plane which most closely match the pathway described by the reaction coordinate diagrams shown above. While the reaction coordinate diagrams both show that the product-formation pathway is energetically downhill, the reaction vectors in Figure 6a show how this can still be an unfavorable pathway. In both **MECP-*syn*** and **MECP-*anti***, the product-formation reaction vector lies downhill from the MECP, but the steepest descent path lies along the reactant-forming vector. While there is no energetic barrier between the two vectors in **MECP-*syn***, the second steepest-descent path for **MECP-*anti*** lies along the product-forming vector. Our calculations suggest that there is a small energetic barrier along the reaction coordinate spanned by the two vectors. Molecules passing through or near **MECP-*syn*** will tend to revert to the reactant while molecules passing through **MECP-*anti*** can continue to the product.

Photo-torquoselectivity

We compared the geometries of several points along the reaction coordinate including the *syn* and *anti* MECPs to determine the origin of the photo-torquoselectivity in the reaction of **2**. We computed non-covalent interaction surfaces using the NCIplot program[67] for each of these geometries. Figure 7 shows the non-covalent interactions in two representative geometries, three steps along each reaction path from the Franck-Condon point.

The NCIplots reveal the presence of weak stereoelectronic effects which govern the photo-torquoselectivity of this reaction. As the reaction proceeds along the *anti* pathway, the fluorines approach the adjacent ladderene hydrogens (F−H distance < 3 Å). As shown in the left half of Figure 7, this results in weakly stabilizing $F^{\delta-}\ldots H^{\delta+}$ interactions. These interactions have been identified as playing a major role in determining the geometric preferences in other fluorinated organic molecules.[68, 69]

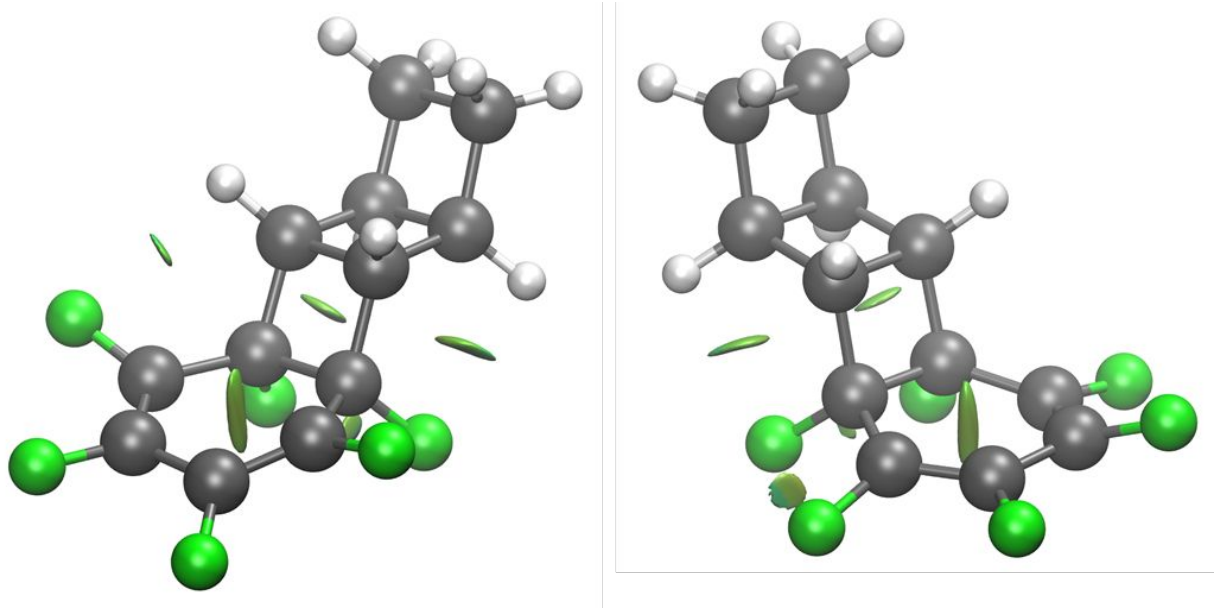

Figure 7. Representative NCIplots for *anti* (left) and *syn* (right) reaction pathways. *Anti* plot shows favorable F...H interaction that stabilizes the *anti* pathway. *Syn* plot shows unfavorable F…F closed-shell repulsion that destabilizes the *syn* pathway.

Figure 7 shows how closed-shell repulsions between adjacent fluorine lone pairs destabilizies the *syn* reaction pathway. These unfavorable interactions are absent along the *anti* reaction pathway as the F−F distances exceed the sum of the van der Waals radii of the two atoms.[70, 71] The combination of the F−F closed-shell repulsion in the *syn* pathway and the F…H stabilization in the *anti* pathway leads to the computed energetic difference of 0.2−0.3 eV (5−7 kcal mol^{-1}). Our dynamics simulations show that this energetic difference results in a significant preference for adopting an *anti* pre-distorted geometry in the excited-state, thereby giving rise to the photo-torquoselective preference for the *anti* configuration in the product.

Conclusions

We have determined the origin of the complete stereoselectivity of a photochemical 4π-electrocyclic ring closing reaction. We have used multiconfigurational quantum mechanical calculations to understand the nature of the vertical excitation and identified a convergence

between multiple computational methods. Static calculations of the reaction path show that the relaxation from the excited to ground state can theoretically occur through one of two pathways that lead to **3** (favored) or **3a** (disfavored). We optimized the corresponding MECPs (**MECP-*syn*** and **MECP-*anti***) and found that the *anti* pathway exhibits two steepest-descent paths, while the *syn* pathway only shows one which leads back to the reactant diene. *Ab initio* molecular dynamics simulations reveal that these destabilizing interactions result in photoexcited molecules of diene **2** having a strong preference for adopting *anti* pre-distorted S_1 geometries. The combination of closed-shell interactions of adjacent fluorine substituents destabilizing the *syn* reaction pathway and $F^{\delta-}\ldots H^{\delta+}$ interactions stabilizing the *anti* pathway result in an energetic difference of as much as 0.3 eV. These cooperative factors block the formation of the **3a,** leading to the observed complete torquoselectivity. This photo−torquoselectivity could be engineered *a priori* through substitutions at key positions on the molecule, which represents a mechanism for stereochemical control of photochemical electrocyclic reactions, and a method for the targeted synthesis of functionalized ladderenes and polyacetylenes. These newly accessible polymers could hold the key to the next generation of organic electronic materials, so a more general development of the photo−torquoselectivity model is currently underway.

Computational Methods

Multiconfigurational methods

CASSCF calculations recover the strong electron correlation which arises from the interaction of multiple degenerate electronic configurations, but is missing the weak, so-called dynamic, component of electron correlation. This is very often recovered by a second-order perturbative correction, CASPT2. To account for the interactions of different electronic states, we have employed a state-averaged CASSCF wavefunction, averaged over the three lowest energy states. To include these same interactions in the CASPT2 calculations, we have used the extended multistate formulation of CASPT2, XMS-CASPT2. The XMS-CASPT2 calculations include an imaginary shift of 0.1 *au* to eliminate intruder states. All CASSCF and XMS-CASPT2 calculations were performed using the OpenMolcas software package.[72, 73]

Excitation energies

We have computed the S_1 vertical excitation energy for **2** using TD-CAM-B3LYP/aug-cc-PVDZ as implemented in the Gaussian 16 software package,[74] and with CASSCF(4,4) and XMS-CASPT2 as implemented in the OpenMolcas software package[72, 73], using both the aug-cc-PVDZ and ANO-S-VDZP basis sets. The CASSCF and XMS-CASPT2 excitation energies are compared to the values computed at the TD-CAM-B3LYP/aug-cc-PVDZ level based on the CASSCF(4,4)/ANO-S-VDZP optimized geometry. An extensive benchmarking study of TD-DFT reports that the range-separated hybrid functional CAM-B3LYP performs well for many small organic molecules, with errors in the range of -0.4 to 0.2 eV, compared to experimental values.[75] The computational cost of *ab initio* MD simulations places restrictions on the size of basis set we can employ, so while we expect the errors in excitation energy for CAM-B3LYP to be larger than those reported in these benchmarking studies, this method should provide a reasonable basis for comparison in the limit of the basis set we have used.

The electronic configurations computed by CASSCF and XMS-CASPT2 should agree with those computed by CAM-B3LYP, though CASSCF typically overestimates the excitation energy due to

a lack of dynamic electron correlation. Significant deviations in the CASSCF and XMS-CASPT2 electronic structure would suggest an insufficient selection of the active space for describing the Franck-Condon region.

Ab initio molecular dynamics

Ab initio molecular dynamics simulations were performed at the SA-3-CASSCF(4,4)/ANO-S-VDZP level using Tully's fewest-switches surface hopping (FSSH) algorithm[65] as implemented in OpenMolcas[72, 73]. The initial conditions were generated from a Wigner distribution of the ground state potential energy surface at 300 K, and were initialized on the first excited state. 256 trajectories were propagated at 300 K for 1 ps with a 1.0 fs time step.

Reaction coordinate diagrams

The reaction coordinate diagrams were computed based on a linear interpolation of internal coordinates between relevant optimized geometries. These interpolations were performed in internal coordinates, rather than Cartesian to minimize the structural changes along the reaction coordinate. The interpolation is achieved by varying the values of all internal coordinates (bond lengths, angles, and dihedrals) in equally-spaced increments from their starting geometry values to those of the end-point geometry. In all cases, the energies of the intermediate geometries were computed at both the CASSCF(4,4)/ANO-L-VTZP and the XMS-CASPT2/ANO-L-VTZP levels. NCIplots were computed using the SCF density computed at the CAM-B3LYP/aug-cc-PVDZ level.

Acknowledgements

The authors wish to thank Dr. Jingbai Li, Mr. Ben Boswell, and Prof. Noah Burns for their insights and helpful discussions. The authors acknowledge the high-performance computing resources and support provided by Northeastern Research Computing (Discovery cluster), the Massachusetts Green High-Performance Computing Center (MGHPCC), and the Army Research Laboratory DoD Supercomputing Resource Center (Excalibur). We are grateful to the Office of Naval Research Multidisciplinary University Research Initiatives (MURI) program (N00014-18-1-2659) for funding support.

References

1. C. Wang, H. Dong, W. Hu, Y. Liu and D. Zhu, *Chemical Reviews*, 2012, **112**, 2208-2267.
2. J. Hou, O. Inganäs, R. H. Friend and F. Gao, *Nature Materials*, 2018, **17**, 119-128.
3. S. A. Lopez, B. Sanchez-Lengeling, J. de Goes Soares and A. Aspuru-Guzik, *Joule*, 2017, **1**, 857-870.
4. L. Han, P. Mandlik, K. H. Cherenack and S. Wagner, *Applied Physics Letters*, 2009, **94**, 162105.
5. G. H. Gelinck, H. E. A. Huitema, E. van Veenendaal, E. Cantatore, L. Schrijnemakers, J. B. P. H. van der Putten, T. C. T. Geuns, M. Beenhakkers, J. B. Giesbers, B.-H. Huisman, E. J. Meijer, E. M. Benito, F. J. Touwslager, A. W. Marsman, B. J. E. van Rens and D. M. de Leeuw, *Nature Materials*, 2004, **3**, 106-110.
6. H. E. A. Huitema, G. H. Gelinck, J. B. P. H. van der Putten, K. E. Kuijk, C. M. Hart, E. Cantatore, P. T. Herwig, A. J. J. M. van Breemen and D. M. de Leeuw, *Nature*, 2001, **414**, 599-599.

7. T. Lv, M. Liu, D. Zhu, L. Gan and T. Chen, *Advanced Materials*, 2018, **30**, 1705489.
8. Y. Wang, L. Sun, C. Wang, F. Yang, X. Ren, X. Zhang, H. Dong and W. Hu, *Chemical Society Reviews*, 2019, **48**, 1492-1530.
9. N. Matsuhisa, X. Chen, Z. Bao and T. Someya, *Chemical Society Reviews*, 2019, **48**, 2946-2966.
10. H. Li, W. Shi, J. Song, H.-J. Jang, J. Dailey, J. Yu and H. E. Katz, *Chemical Reviews*, 2019, **119**, 3-35.
11. J. Huang, G. Zhang, X. Zhao, X. Wu, D. Liu, Y. Chu and H. E. Katz, *Journal of the American Chemical Society*, 2017, **139**, 12366-12369.
12. C. Goldmann, S. Haas, C. Krellner, K. P. Pernstich, D. J. Gundlach and B. Batlogg, *Journal of Applied Physics*, 2004, **96**, 2080-2086.
13. E. A. Schiff, R. I. Devlen, H. T. Grahn, J. Tauc and S. Guha, *Applied Physics Letters*, 1989, **54**, 1911-1913.
14. A. L. Briseno, R. J. Tseng, M. M. Ling, E. H. L. Falcao, Y. Yang, F. Wudl and Z. Bao, *Advanced Materials*, 2006, **18**, 2320-2324.
15. L. Lu, T. Zheng, Q. Wu, A. M. Schneider, D. Zhao and L. Yu, *Chemical Reviews*, 2015, **115**, 12666-12731.
16. G. Li, R. Zhu and Y. Yang, *Nature Photonics*, 2012, **6**, 153-161.
17. N. C. Davy, M. Sezen-Edmonds, J. Gao, X. Lin, A. Liu, N. Yao, A. Kahn and Y.-L. Loo, *Nature Energy*, 2017, **2**, 17104.
18. A. W. Lang, Y. Li, M. De Keersmaecker, D. E. Shen, A. M. Österholm, L. Berglund and J. R. Reynolds, *ChemSusChem*, 2018, **11**, 854-863.
19. S. D. Kim, B. Lee, T. Byun, I. S. Chung, J. Park, I. Shin, N. Y. Ahn, M. Seo, Y. Lee, Y. Kim, W. Y. Kim, H. Kwon, H. Moon, S. Yoo and S. Y. Kim, *Science Advances*, 2018, **4**, eaau1956.
20. D. Zhang, T. Huang and L. Duan, *Advanced Materials*, 2019, 1902391.
21. H. Shirakawa, E. J. Louis, A. G. MacDiarmid, C. K. Chiang and A. J. Heeger, *Journal of the Chemical Society, Chemical Communications*, 1977, DOI: 10.1039/C39770000578, 578-580.
22. S. Yang and E. Ruckenstein, *Concentrated Emulsion Polymerization*, 2019.
23. S.-H. Jeong, S. Ahn and T.-W. Lee, *Macromolecular Research*, 2019, **27**, 2-9.
24. T. P. Kaloni, P. K. Giesbrecht, G. Schreckenbach and M. S. Freund, *Chemistry of Materials*, 2017, **29**, 10248-10283.
25. A. M. Saxman, R. Liepins and M. Aldissi, *Progress in Polymer Science*, 1985, **11**, 57-89.
26. T. Yamabe, K. Tanaka, H. Terama-E, K. Fukui, H. Shirakawa and S. Ikeda, *Synthetic Metals*, 1980, **1**, 321-327.
27. M. Springborg, *Journal of the American Chemical Society*, 1999, **121**, 11211-11216.
28. D. A. Dixon and B. E. Smart, in *Selective Fluorination in Organic and Bioorganic Chemistry*, American Chemical Society, 1991, vol. 456, ch. 2, pp. 18-35.
29. Z. Chen, X. Zhu, J. Yang, J. A. M. Mercer, N. Z. Burns, T. J. Martinez and Y. Xia, *Nature Chemistry*, 2020, **12**, 302-309.
30. B. Benjamin R., M. Carl M. F., C. Jordan M, J. Zexin, R. Joseph A. H., L. Kurt P., C. Lynette, X. Yan, L. Steven and B. Noah Z., *Mechanochemical Synthesis of Elusive Fluorinated Polyacetylene*, 2019.
31. R. B. Woodward and R. Hoffmann, *Journal of the American Chemical Society*, 1965, **87**, 395-397.

32. P. N. Carlsen, T. J. Mann, A. H. Hoveyda and A. J. Frontier, *Angewandte Chemie International Edition*, 2014, **53**, 9334-9338.
33. X. Yan and X. Hu, *The Journal of Organic Chemistry*, 2014, **79**, 5282-5286.
34. P. Magnus, W. A. Freund, E. J. Moorhead and T. Rainey, *Journal of the American Chemical Society*, 2012, **134**, 6140-6142.
35. D. Knueppel and S. F. Martin, *Tetrahedron*, 2011, **67**, 9765-9770.
36. D. Knueppel and S. F. Martin, *Angewandte Chemie International Edition*, 2009, **48**, 2569-2571.
37. W.-D. Z. Li, W.-G. Duo and C.-H. Zhuang, *Organic Letters*, 2011, **13**, 3538-3541.
38. A. Y. Bitar and A. J. Frontier, *Organic Letters*, 2009, **11**, 49-52.
39. S. Gao, Q. Wang and C. Chen, *Journal of the American Chemical Society*, 2009, **131**, 1410-1412.
40. W. He, J. Huang, X. Sun and A. J. Frontier, *Journal of the American Chemical Society*, 2008, **130**, 300-308.
41. S. P. Waters, Y. Tian, Y.-M. Li and S. J. Danishefsky, *Journal of the American Chemical Society*, 2005, **127**, 13514-13515.
42. N. G. Rondan and K. N. Houk, *Journal of the American Chemical Society*, 1985, **107**, 2099-2111.
43. A. B. Buda, Y. Wang and K. N. Houk, *The Journal of Organic Chemistry*, 1989, **54**, 2264-2266.
44. C. W. Jefford, G. Bernardinelli, Y. Wang, D. C. Spellmeyer, A. Buda and K. N. Houk, *Journal of the American Chemical Society*, 1992, **114**, 1157-1165.
45. D. P. Canterbury, I. R. Herrick, J. Um, K. N. Houk and A. J. Frontier, *Tetrahedron*, 2009, **65**, 3165-3179.
46. K. Honda, S. A. Lopez, K. N. Houk and K. Mikami, *The Journal of Organic Chemistry*, 2015, **80**, 11768-11772.
47. B. A. Boon, A. G. Green, P. Liu, K. N. Houk and C. A. Merlic, *The Journal of Organic Chemistry*, 2017, **82**, 4613-4624.
48. J. Franck and E. G. Dymond, *Transactions of the Faraday Society*, 1926, **21**, 536-542.
49. B. G. Levine, C. Ko, J. Quenneville and T. J. MartÍnez, *Molecular Physics*, 2006, **104**, 1039-1051.
50. F. Plasser, S. A. Mewes, A. Dreuw and L. González, *Journal of Chemical Theory and Computation*, 2017, **13**, 5343-5353.
51. T. Yanai, D. P. Tew and N. C. Handy, *Chemical Physics Letters*, 2004, **393**, 51-57.
52. B. O. Roos, *Advances in Chemical Physics*, 1987, DOI: doi:10.1002/9780470142943.ch7

10.1002/9780470142943.ch7, 399-445.
53. A. A. Granovsky, *The Journal of Chemical Physics*, 2011, **134**, 214113.
54. T. Shiozaki, W. Győrffy, P. Celani and H.-J. Werner, *The Journal of Chemical Physics*, 2011, **135**, 081106.
55. M. Schreiber, M. R. Silva-Junior, S. P. A. Sauer and W. Thiel, *The Journal of Chemical Physics*, 2008, **128**, 134110.
56. D. Jacquemin, V. Wathelet, E. A. Perpète and C. Adamo, *Journal of Chemical Theory and Computation*, 2009, **5**, 2420-2435.
57. A. J. Atkins, F. Talotta, L. Freitag, M. Boggio-Pasqua and L. González, *Journal of Chemical Theory and Computation*, 2017, **13**, 4123-4145.
58. P. Kimber and F. Plasser, *Physical Chemistry Chemical Physics*, 2020, **22**, 6058-6080.

59. C. Angeli, *Journal of Computational Chemistry*, 2009, **30**, 1319-1333.
60. M. Boggio-Pasqua, M. J. Bearpark, M. Klene and M. A. Robb, *The Journal of Chemical Physics*, 2004, **120**, 7849-7860.
61. W. T. Borden and E. R. Davidson, *Accounts of Chemical Research*, 1996, **29**, 67-75.
62. B. O. Roos, K. Andersson and M. P. Fülscher, *Chemical Physics Letters*, 1992, **192**, 5-13.
63. H. Lischka, D. Nachtigallová, A. J. A. Aquino, P. G. Szalay, F. Plasser, F. B. C. Machado and M. Barbatti, *Chemical Reviews*, 2018, **118**, 7293-7361.
64. A. L. Thompson and T. J. Martínez, *Faraday Discussions*, 2011, **150**, 293-311.
65. J. C. Tully, *The Journal of Chemical Physics*, 1990, **93**, 1061-1071.
66. I. Fdez. Galván, M. G. Delcey, T. B. Pedersen, F. Aquilante and R. Lindh, *Journal of Chemical Theory and Computation*, 2016, **12**, 3636-3653.
67. J. Contreras-García, E. R. Johnson, S. Keinan, R. Chaudret, J.-P. Piquemal, D. N. Beratan and W. Yang, *Journal of Chemical Theory and Computation*, 2011, **7**, 625-632.
68. L. H. Simões and R. A. Cormanich, *European Journal of Organic Chemistry*, 2020, **2020**, 501-505.
69. T. V. Rybalova and I. Y. Bagryanskaya, *Journal of Structural Chemistry*, 2009, **50**, 741-753.
70. A. Bondi, *The Journal of Physical Chemistry*, 1964, **68**, 441-451.
71. M. Mantina, A. C. Chamberlin, R. Valero, C. J. Cramer and D. G. Truhlar, *The Journal of Physical Chemistry A*, 2009, **113**, 5806-5812.
72. I. Fdez. Galván, M. Vacher, A. Alavi, C. Angeli, F. Aquilante, J. Autschbach, J. J. Bao, S. I. Bokarev, N. A. Bogdanov, R. K. Carlson, L. F. Chibotaru, J. Creutzberg, N. Dattani, M. G. Delcey, S. S. Dong, A. Dreuw, L. Freitag, L. M. Frutos, L. Gagliardi, F. Gendron, A. Giussani, L. González, G. Grell, M. Guo, C. E. Hoyer, M. Johansson, S. Keller, S. Knecht, G. Kovačević, E. Källman, G. Li Manni, M. Lundberg, Y. Ma, S. Mai, J. P. Malhado, P. Å. Malmqvist, P. Marquetand, S. A. Mewes, J. Norell, M. Olivucci, M. Oppel, Q. M. Phung, K. Pierloot, F. Plasser, M. Reiher, A. M. Sand, I. Schapiro, P. Sharma, C. J. Stein, L. K. Sørensen, D. G. Truhlar, M. Ugandi, L. Ungur, A. Valentini, S. Vancoillie, V. Veryazov, O. Weser, T. A. Wesołowski, P.-O. Widmark, S. Wouters, A. Zech, J. P. Zobel and R. Lindh, *Journal of Chemical Theory and Computation*, 2019, **15**, 5925-5964.
73. F. Aquilante, J. Autschbach, R. K. Carlson, L. F. Chibotaru, M. G. Delcey, L. De Vico, I. Fdez. Galván, N. Ferré, L. M. Frutos, L. Gagliardi, M. Garavelli, A. Giussani, C. E. Hoyer, G. Li Manni, H. Lischka, D. Ma, P. Å. Malmqvist, T. Müller, A. Nenov, M. Olivucci, T. B. Pedersen, D. Peng, F. Plasser, B. Pritchard, M. Reiher, I. Rivalta, I. Schapiro, J. Segarra-Martí, M. Stenrup, D. G. Truhlar, L. Ungur, A. Valentini, S. Vancoillie, V. Veryazov, V. P. Vysotskiy, O. Weingart, F. Zapata and R. Lindh, *Journal of Computational Chemistry*, 2016, **37**, 506-541.
74. G. W. T. M. J. Frisch, H. B. Schlegel, G. E. Scuseria, M. A. Robb, J. R. Cheeseman, G. Scalmani, V. Barone, G. A. Petersson, H. Nakatsuji, X. Li, M. Caricato, A. V. Marenich, J. Bloino, B. G. Janesko, R. Gomperts, B. Mennucci, H. P. Hratchian, J. V. Ortiz, A. F. Izmaylov, J. L. Sonnenberg, D. Williams-Young, F. Ding, F. Lipparini, F. Egidi, J. Goings, B. Peng, A. Petrone, T. Henderson, D. Ranasinghe, V. G. Zakrzewski, J. Gao, N. Rega, G. Zheng, W. Liang, M. Hada, M. Ehara, K. Toyota, R. Fukuda, J. Hasegawa, M. Ishida, T. Nakajima, Y. Honda, O. Kitao, H. Nakai, T. Vreven, K. Throssell, J. A. Montgomery, Jr., J. E. Peralta, F. Ogliaro, M. J. Bearpark, J. J. Heyd, E. N. Brothers, K. N. Kudin, V. N. Staroverov, T. A. Keith, R. Kobayashi, J. Normand, K. Raghavachari, A. P. Rendell, J. C.

Burant, S. S. Iyengar, J. Tomasi, M. Cossi, J. M. Millam, M. Klene, C. Adamo, R. Cammi, J. W. Ochterski, R. L. Martin, K. Morokuma, O. Farkas, J. B. Foresman, D. J. Fox, *Journal*, 2016, **Revision A.03**.

75. M. Caricato, G. W. Trucks, M. J. Frisch and K. B. Wiberg, *Journal of Chemical Theory and Computation*, 2010, **6**, 370-383.